



Experimental investigation of rotational behavior of pseudo-ductile adhesive angle joints exhibiting variable strain rate

Ghazaleh Eslami, A. Vahid Movahedi-Rad, Thomas Keller^{*}

Composite Construction Laboratory (CCLab), École Polytechnique Fédérale de Lausanne (EPFL), Switzerland

ARTICLE INFO

Handling Editor: Prof. Ole Thomsen

Keywords:

Pseudo-ductile adhesive
Adhesive composite joint
Variable strain rate
Moment-rotation characteristic

ABSTRACT

Pseudo-ductile behavior in composite structural frames can be achieved by enabling their beam-column joints to exhibit nonlinear structural response due to progressive damage, by using pseudo-ductile adhesives. This study investigates the static behavior of a novel pseudo-ductile bonded-bolted angle joint with a bolt at the geometric centroid of the joint. A pseudo-ductile elastomer adhesive is used which is notably sensitive to the strain rate. The bolt ensures structural integrity and produces pure torsional moments in the adhesive planes. This configuration induces nonuniform strain rates in the adhesive layers in the radial direction, i.e., from the center outwards. The experimental results reveal that under the nonuniform shear strain distribution, the initial stiffness, yield rotation, and maximum torsion exhibit an increasing trend with strain rate, while maximum rotation decreases. An analytical model was developed using stress-strain relations obtained from single-lap joints with uniform stress distribution to predict the angle joint responses. The analytical model overestimates the initial joint stiffness due to the nonuniform stress distribution but shows good agreement for strength and post-yield behavior. Lastly, the angle joint exhibits the lowest ductility ratios compared to linear lap joints, showing that the pseudo-ductile adhesive capacity may not be fully utilized in the angle configuration.

1. Introduction

The escalating global demand for lightweight yet durable structural components has led to the adoption of pultruded glass fiber-polymer composite laminates in a variety of construction applications. Composite laminates confer significant benefits, including a high strength-to-weight ratio, corrosion resistance, and expedited erection [1]. Nevertheless, the intrinsic brittleness of glass composite laminates may result in catastrophic failure of composite structures under diverse loading conditions [2]. To circumvent such catastrophic failures, enhancing the ductility of composite structures is imperative, which can be achieved by enhancing their connections, such as bridge deck-girders or beam-column connections, through the introduction of pseudo-ductility. Pseudo-ductility in this respect is understood as the nonlinear response caused by progressive damage and associated viscoelastic energy dissipation that can occur on the system, member, joint, or material level [3]. Options to achieve pseudo-ductility in the connections are the use of either adhesive-bolt combinations [4] or pseudo-ductile adhesives [5]. Pseudo-ductility in the connections augments the performance of fiber-polymer composite pultruded structures, mainly by increasing

their energy dissipation capacity [6].

Since the 1990s, researchers have been investigating hybrid and bolted pultruded beam-column connection configurations with the aim of attaining superior mechanical performance to conventional bolted joints. Bank et al. [7,8] conducted comparative analyses of rotational stiffness, strength, and failure modes for eight full-scale glass composite beam-column connections. Among those, six connections comprised different configurations of pultruded angles and built-up components bolted to both beams and columns, while the remaining two were hybrid bolted-bonded beam-column connections using an epoxy adhesive. They found that the studied hybrid connections demonstrated higher rotational stiffness and moment strength. Subsequently, Smith et al. [9] conducted an experimental study on the behavior of the hybrid connections proposed by Bank et al. with pultruded glass composite I- and box-section profiles. Their findings emphasized the superior performance of box-section connections in terms of strength and stiffness relative to I-section connections. The considerable gains in stiffness and strength of glass composite connections obtained using adhesive bonding inspired Carrion et al. [10] to conduct experimental studies on a beam-column box-section connection employing a T-shaped monolithic

^{*} Corresponding author.

E-mail addresses: ghazaleh.eslami@epfl.ch (G. Eslami), abdolvahid.movahedirad@epfl.ch (A.V. Movahedi-Rad), thomas.keller@epfl.ch (T. Keller).

connector, referred to as "cuff" connection, utilizing a high-strength epoxy. They determined the optimum thickness of their cuff connection that allowed the frame to achieve the full flexural capacity of the pultruded box beams. In 2017, Ascione et al. [11] studied four full-scale glass composite epoxy-bonded I-profile beam-column connections subjected to static loads, focusing on connection location and column strengthening methodologies. The connections composed of seat angles and column stiffeners attained the highest moment capacity. Meanwhile, a primary drawback of adhesive connections identified in the studies was the brittle failure mode, such as adherend or adhesive interface failure, making them less appropriate for being used in structures. The observed limited deformation capacity renders the examined adhesives unsuitable for earthquake resistance as well. To mitigate brittle failure modes of adhesive connections, Ascione et al. [12] modified the proposed connection in Ref. [11] to achieve pseudo-ductile failure modes. The modification entailed wrapping the connection at specific locations using a carbon fiber fabric, employing epoxy resin and wet lay-up technique. Their strengthened connection exhibited a pseudo-ductile load-deflection response.

Pseudo-ductile behavior in pultruded structures can even be achieved with simpler joint configurations such as cleated joints [13]. Qureshi et al. [14] studied glass composite beam-to-column connections featuring steel and composite cleats, discovering enhanced torsional moment capacity and stiffness at the expense of diminished rotational deformation. Ascione et al. [15] explored the effect of the bonded area dimensions on the flexural and shear behavior of epoxy adhesive beam and column connections using L-shaped profiles on the top and the bottom of the beam. Their findings indicated that the extension of the bonded area influenced the strength but not the stiffness of the connections, while the adhesive layer experienced torsional moments.

The two main concerns regarding the beam-column connections investigated in prior experiments involve the durability of hybrid connections and the required ductility. Durability concerns in hybrid connections stem from the need for drilling into composite materials for joint installation [16]. Additionally, neither the brittle adhesive joints nor the hybrid joints using brittle adhesives exhibited a sufficient amount of ductility required for seismic resistant design [17]. Implementing pseudo-ductile adhesives in composite connections can help alleviate these concerns. Unlike in brittle adhesives, experiments on linear pseudo-ductile adhesive lap joint connections under tension have shown that the stresses are uniformly distributed over the bonded surfaces [18]. Pseudo-ductile adhesives create a partial composite action between the adherends, and can thus also be used for stress mitigation [19]. However, the mechanical properties of pseudo-ductile adhesives are sensitive to the applied strain rate [20]. Under low strain rates, pseudo-ductile adhesives exhibit lower stiffness and reduced yield strength, while they can achieve high failure displacement and strength due to molecular chain realignment and stretching into the applied displacement direction [21].

While pseudo-ductile adhesives have previously been examined in composite lap joints, their applications in beam-to-column joints, along with their strain rate-dependent stiffness, moment-rotation resistance, and overall performance have not yet been addressed. The adhesive layer in the studied lap joints experienced a constant strain rate and a uniform stress distribution along the overlap throughout the experiments. However, as noted earlier, in typical bonded beam-column joints (such as those studied in Ref. [15]), the adhesive layers will be subjected to torsional moments, inducing variable strain rates and consequently, nonuniform stress distributions in the radial direction from the rotational center. Taking this into consideration, the current study investigates the behavior of a novel adhesive angle double-lap joint under torsional moments, aiming to develop an analytical model with low computational cost for predicting the load bearing capacity under nonuniform stress distribution in the adhesive layers. The basic rate-dependent stress-strain relationships of the adhesive were derived from experiments on adhesive single-lap joints exhibiting a uniform

stress distribution. Three different external displacement rates were applied to the angle joints to obtain their moment-rotation responses under different internal strain rate ranges in the adhesive layers. Based on the rate-dependent stress-strain relationships obtained from the single-lap joints, the torsional moment capacities of the angle joints under variable internal strain rate and associated nonuniform stress distributions could be predicted.

2. Angle joint concept and experimental program

A novel bonded-bolted angle double-lap joint was designed where a central bolt transfers the section forces, permitting relative joint rotations, while blocking relative translations in the adherend plane. The two pseudo-ductile adhesive layers resist the rotations and thus experience pure torsion, resulting in a nonuniform strain rate in the radial direction. An analytical model was suggested to predict the mechanical performance of the pseudo-ductile adhesive under nonuniform strain rate, utilizing strain rate-dependent stress-strain responses as input data. The input data were obtained from linear single-lap joints according to ASTM D1002-10 [22], which exhibited a uniform strain rate and stress distribution along the overlap.

2.1. Angle joint experimental approach

The angle joint consists of an inner laminate perpendicularly connected to two outer laminates by a pseudo-ductile adhesive, forming an isosceles right triangle (Fig. 1(a)). Fig. 1(b) schematically represents the symmetric deformation of each of the inner and outer laminates, θ , under an applied load, F . The load, F , can be decomposed into internal shear and axial loads in the laminates, denoted as F_1 and F_2 , respectively. The bolt placed at the centroid of the adhesively bonded area transfers these internal forces between inner and outer laminates while preventing relative in-plane displacements. The adhesive joint area in Fig. 1(b) is represented by a rotational spring, indicating its resistance to rotation. Fig. 1(c) presents free-body diagrams of the specimen components and the decomposition of the loads acting on them. Additionally, Fig. 1(d)–(f) demonstrate the internal force and moment diagrams of each specimen component shown in Fig. 1(c). Each outer laminate carries half the load borne by the inner laminate. The relationship between F_1 , F_2 , and F can be determined as follows:

$$F_1 = F \times \cos(45 + \theta) \quad \text{Eq. (1)}$$

$$F_2 = F \times \sin(45 + \theta) \quad \text{Eq. (2)}$$

By considering equilibrium in the inner laminate, the internal torsional moment borne by the adhesive layers, T , can be calculated as follows:

$$T = F_1 \times L_1 = F \times \cos(45 + \theta) \times (L - a_1 - a_2) \quad \text{Eq. (3)}$$

where L_1 is the distance between the point of load application and the bolt, L is the laminates' length, a_1 is the distance of the point of load application to the edge of the laminate, and a_2 is the bolt distance to the edge of the laminate, all shown in Fig. 1(a).

2.2. Specimen geometry and fabrication

2.2.1. Single-lap experiments

The adhesive single-lap joint specimens were fabricated according to Ref. [22] as shown in Fig. 2 from two steel sheets of 1.5 mm thickness and bonded together over a length of 13 mm. The steel sheets, measuring 101.5 mm \times 25.5 mm \times 1.5 mm, were cut from a plate of 1.5 mm thickness using a waterjet. The shear area of the steel sheets was scratched with a grade 60 sandpaper according to ASTM D2651-01 [23] and then was cleaned with a Sika product (Sika® ADPrep) [24]. The pseudo-ductile adhesive was then applied to the shear area using a

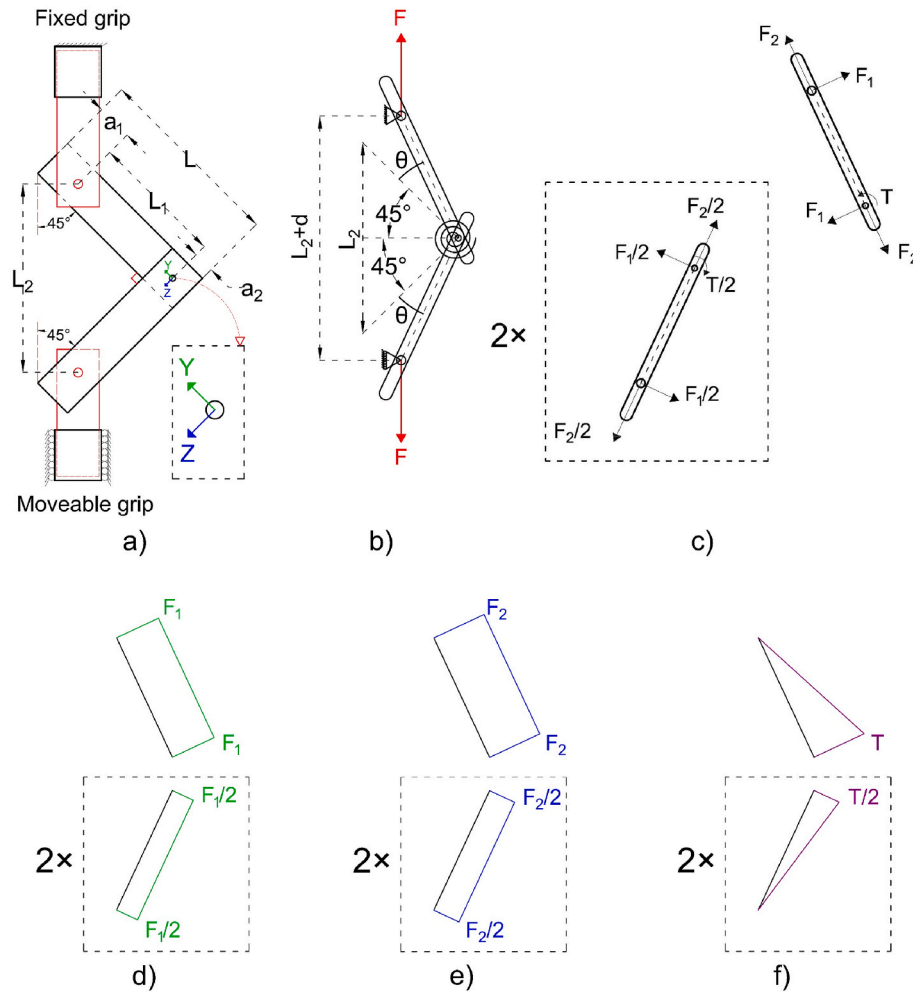


Fig. 1. Schematic representation of angle joint specimen a) fixed in machine b) deformed state c) acting load decomposition d) internal shear diagram e) internal axial force diagram f) internal bending moment diagram.

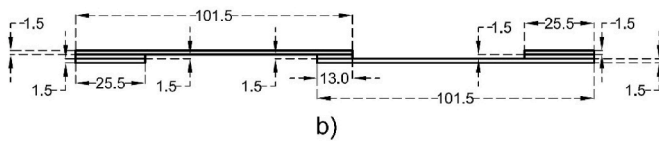
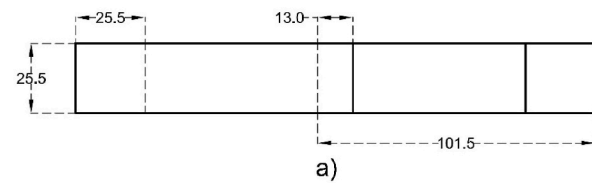


Fig. 2. Single-lap specimen dimensions according to ASTM D1002 [22] a) top view, b) side view.

mixing gun, with two steel beads of 1.5 mm diameter placed in the shear (bonding) area to guarantee the targeted layer thickness. To have the same total thickness at the ends of the specimen as in the middle, steel tabs measuring 25.5 mm \times 25.5 mm were bonded with an epoxy adhesive (Sikadur-330) to the ends of the steel sheet adherends. The tabs were made of the same steel material as the steel adherends. The joints were then stored for five days under ambient laboratory conditions (23

$\pm 2^\circ\text{C}$ and $38 \pm 10\%$ relative humidity) prior to the experiments due to organizational reasons. Previous results of differential scanning calorimetry (DSC) showed that, under these conditions, the adhesive was cured to 99% after 4 h already [20]. The adhesive was thus fully cured after five days.

2.2.2. Angle joint experiments

The angle joint specimens comprised an inner laminate and two

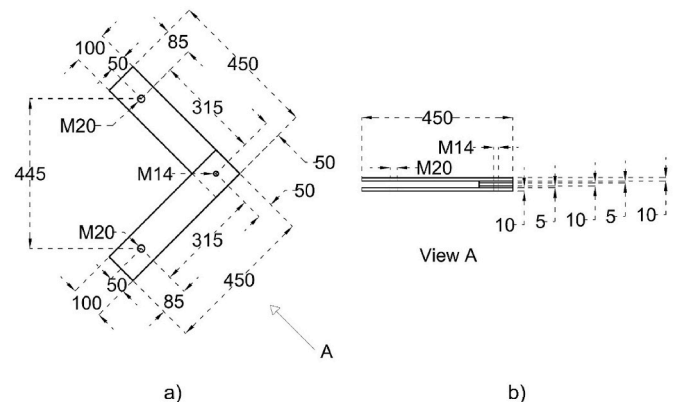


Fig. 3. Angle joint specimen dimensions in mm from a) top view, b) side view.

outer laminates, each measuring 450 mm × 100 mm × 10 mm in length, width, and thickness, respectively as shown in Fig. 3. A joint area of 100 mm × 100 mm, with an adhesive thickness of either 5 mm or 2.5 mm, to represent typical applications in composite bridge and building construction [25,26], was then considered. To fabricate the angle joints, the composite laminates surface was roughened with sandpaper to remove the polyester layer, revealing the mat layer at a depth of about 0.5 mm. A thin epoxy adhesive layer (Sikadur-330) was then applied to the scratched surface as a bonding promoter using a construction spatula, leaving some marks on the surface. The epoxy layer was left to cure for 4 h at 60 °C [27]. The inner and outer laminates were then adhesively bonded using the pseudo-ductile adhesive which was applied by a mixing gun. Four steel beads of 5 mm or 2.5 mm in diameter were placed in the bonding area to ensure the desired adhesive layer thickness. After applying the adhesive for each lap, the specimen was cured for one day under ambient laboratory conditions (20 ± 3 °C and 38 ± 10% relative humidity) to achieve full cure (see above). Lastly, the joints were stored in the same room for five days due to organizational reasons before the experiments. After these five days, the center of the adhesively bonded area was drilled, at a distance of 50 mm from the laminate's edge, and pinned with a 14 mm diameter bolt.

2.3. Materials

The pseudo-ductile structural adhesive based on acrylic double performance (ADP) polymer technology, SikaFast®-555L10 (L05), supplied by Sika, Switzerland was used in this study. This two-part adhesive system consists of two components, SikaFast®-555 and SikaFast®-555 L10, which are mixed at a ratio of 10:1 (by volume). Elastic moduli ranging from 340 MPa to 780 MPa were measured in standardized dog-bone specimens, varying with the applied displacement rates of 0.1 mm/s up to 10 mm/s displacement rates [28].

In single-lap adhesively bonded specimens, a DIN EN 1.4034 stainless steel (AISI 420/X46Cr13) plate was used for the adherends. The material was selected according to the requirements of ASTM D1002-10 [19].

The laminates used in the angle joint specimens were made of glass fiber-polymer composites provided by Fiberline Denmark, and were composed of E-glass fibers in an isophthalic polyester resin matrix with a fiber content of 60% by weight. The laminate structure comprised 70% unidirectional rovings in the core and two outer layers of combined mats, with a polyester surface veil applied to the exterior surfaces. According to the manufacturer, the laminates' longitudinal elastic modulus and tensile strength were 28 GPa and 240 MPa, respectively [29]. Grade 80 stainless steel bolts were used, with an unthreaded length of 35 mm.

2.4. Setup, instrumentation, and experimental procedure

2.4.1. Single-lap experiments

To conduct tension loading experiments, single-lap shear specimens were fixed at their tabs in the grips of an MTS 25 kN universal testing machine. The experiments were conducted in a displacement-controlled mode, with six applied tensile displacement rates of 0.01, 0.05, 0.1, 0.5, 1.0, and 5.0 mm/s, all referring to the machine's cross-head displacement. The relative displacements in the joint area were measured using a Digital Image Correlation (DIC) system. The DIC system was placed in front of the experimental setup and monitored the movement of the speckles on both steel sheets. Three specimens, each designated by the specimen type (SL), loading rate (0.01, 0.05, 0.1, 0.5, 1.0, and 5.0), and joint replication (1–3), were investigated at each displacement rate. As an example, the designation "SL-0.01-1" represents the first single-lap specimen subjected to a displacement rate of 0.01 mm/s.

2.4.2. Angle joint experiments

Displacement-controlled monotonic experiments were conducted in a laboratory setting at room temperature (19 ± 3 °C) using a Walter +

Bai type LFV universal testing machine with a maximum capacity of 200 kN in tension and compression and a maximum displacement of 200 mm. Two steel fixtures were placed in the top and bottom grips of the machine, to which the inner laminate and outer laminates were hinged using a 20 mm bolt, allowing for the free rotation of the end bolts, as shown in Fig. 4. The nuts were hand-tightened to prevent the bolts from being pre-stressed. The machine applied the displacement with the desired external rate and measured the resulting loads. The rotation of the laminates was recorded using two inclinometers with an accuracy of 0.001 radians, one attached to the middle of the inner laminate, inclinometer_1, and the other to the middle of an outer laminate, inclinometer_2. To measure the adhesive layer deformations in the angle joint, a two-camera 3D DIC system was used. These cameras enabled the tracking of specimens' motion in 3D space (stereo vision) with an accuracy of ±0.01%. A random speckle pattern was applied on the measured surfaces, i.e., edge of the joint area, using both white and black spray in the dashed-line rectangle in Fig. 4. The DIC measured area was illuminated with a non-heating LED EFFILUX white light. The light was positioned at a fixed angle and distance from the specimens to provide consistent illumination during the experiments. The post-processing of the results was carried out using Vic-3D software from Correlated Solutions Inc. Furthermore, the specimens were photographed by two additional cameras to monitor them during the experiments.

Three external displacement rates of 0.1, 0.5, and 2.0 mm/s, selected according to the CUREE protocol [30], were applied by the machine to the angle joint specimens. During each experiment, the machine applied a constant downward displacement rate to the bottom grip, thus resulting in a range of variable internal strain rates in the joint area.

Three specimens were examined for each displacement rate and thickness of the adhesive layer. The joint designations comprised the joint loading type (M), adhesive thickness (t5 or t2.5), loading rate (0.1, 0.5, 2.0), and joint replication (a, b, c, or d). For example, the

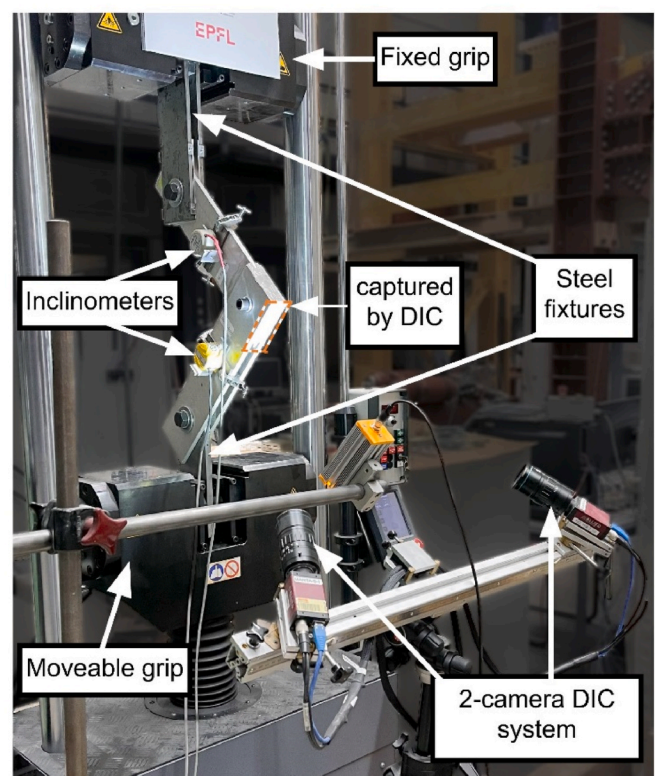


Fig. 4. Angle-joint specimen experiment setup with two-camera 3D DIC measurement.

designation "M-t5-0.1a" represents the first angle joint subjected to monotonic loading with an adhesive thickness of 5 mm at a rate of 0.1 mm/s.

2.5. Experimental results

2.5.1. Single-lap experiments

2.5.1.1. Stress-strain responses. The single-lap experiments investigated the shear stress-strain behavior of the pseudo-ductile adhesive over a wide range of displacement rates. The shear stress, τ , and shear strain, γ , values were calculated from the measured force and deformations using Eq. (4) and Eq. (5), assuming a uniform stress distribution along the overlap.

$$\tau = \frac{F}{A_s} \quad \text{Eq. (4)}$$

$$\gamma = \frac{d}{t_s} \quad \text{Eq. (5)}$$

where F is the load recorded by the machine, A_s is the joint area, d is the joint displacement, and t_s is the adhesive layer thickness in single-lap joint specimens, equaling 1.5 mm. Fig. 5(a) shows the stress-strain curves obtained from Eqs. (4) and (5) for the selected specimens under the applied displacement rates of 0.01, 0.05, 0.1, 0.5, 1.0, and 5.0 mm/s.

The effects of the applied strain rates on the shear behavior of the specimens were studied by analyzing the parameters extracted from the stress-strain curves. The shear modulus, G_I , was calculated from the slope of a tangent line to the initial section of each specimen's stress-strain curve. The yield points were considered as the points where the tangent line's slope dropped to 20% of the initial slope, and accordingly, the yield stress, τ_y , as well as its corresponding value of strain, γ_y , were obtained. Furthermore, the post-yield modulus, G_2 , was calculated from the slope of a line between the yield point and the maximum stress, the strength was defined as the maximum stress, τ_{\max} , and its corresponding value of strain, γ_{\max} , as the maximum strain. Table 1 summarizes the average values and standard errors of the extracted parameters for each set of specimens subjected to the same applied displacement rates. It can be seen that all parameters increased with increasing the strain rate except for the post-yield modulus and the maximum strain, which decreased as the strain rate increased. The obtained shear strain values from DIC results along the overlap of the joint are shown in Fig. 5 (b) when the stress was equal to 6 MPa. The shear strain values confirm a uniform strain distribution along the joint area for all displacement rates. For each displacement rate, \dot{d} , the corresponding uniform strain rate, $\dot{\gamma}$, was calculated as follows:

$$\dot{\gamma} = \frac{\dot{d}}{t_s} \quad \text{Eq. (6)}$$

2.5.1.2. Failure mode. Fig. 6 illustrates the failure surfaces of the single-lap joint area for selected specimens subjected to six different displacement rates. All specimens failed within the adhesive layer, which, based on the classification provided by Ref. [31], can be considered as a mixed mode of cohesive failure and adhesive failure. However, the majority of the fracture surfaces exhibit cohesive failure.

2.5.2. Angle joint experiments

2.5.2.1. Rotation rate in the specimens. This section studies the laminate rotation angle and laminate rotation rate, stemming from the external displacement applied by the machine to the angle joint specimens. The rotation angle was measured relative to the initial undeformed state using the two installed inclinometers (Fig. 4). Fig. 7(a) curves represent the clockwise (positive) and counterclockwise (negative) rotations of the inner and outer laminates, respectively. The identical rotation angles of inner and outer laminates at each load level verify the rotational symmetry around the connecting bolt within the joint area. Therefore, considering the symmetry in rotation and geometry of the specimen, the relation between the edges of the right triangle formed between the bottom load application point, the bolt, and the midpoint between the top and bottom application points could be written as follows (according to Fig. 1 (b)):

$$L_1 \times \sin(45 + \theta) = \frac{L_2 + d}{2} \quad \text{Eq. 7}$$

where L_2 is the vertical distance between the top and bottom load application points (Fig. 1 (a)), and d is the machine displacement. Then, by rearranging Eq. (7), and substituting the values of L_1 and L_2 from Fig. 3, the laminate rotation angle can be derived from the machine displacement, as follows:

$$\theta = \left[\arcsin \left(\frac{445 + d}{2 \times 315} \right) - 45^\circ \right] \times \left(\frac{\pi}{180} \right) \text{ rad} \quad \text{Eq. 8}$$

Fig. 7(b) illustrates the rotation angles calculated by Eq. (8), represented by the dashed lines, and the rotation angles of the inner laminate, measured by the inclinometer depicted by the solid lines, over time for specimens subjected to different displacement rates. The slope of these curves corresponds to the laminate rotation rate of each specimen, denoted as $\dot{\theta}$. The good agreement between the inclinometer rotation measurements and the calculated rotations obtained from Eq. (8) further validates the calculations and symmetric deformation of the joint area.

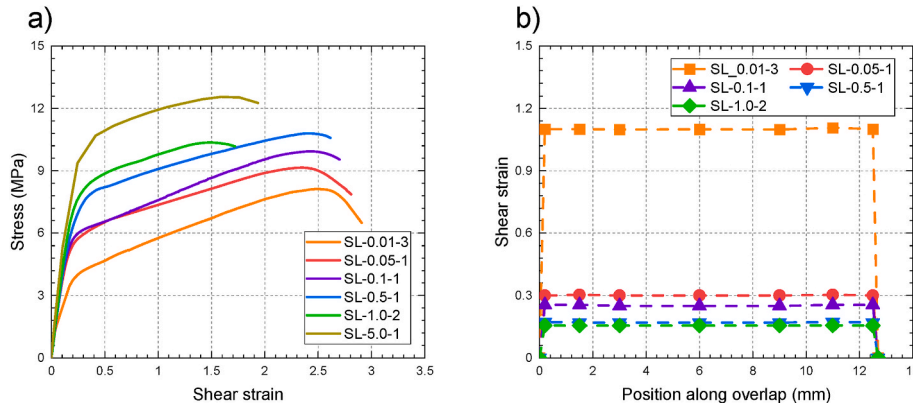


Fig. 5. a) Shear stress-strain relation under different applied displacement rates for single-lap joints, b) shear strain distribution along single-lap joint overlap under different applied displacement rates at shear stress of 6 MPa.

Table 1
Single-lap joint experimental results.

Sp. name	\dot{d} (mm/s)	$\dot{\gamma}$ (1/s)	G_I (MPa)	γ_y	τ_y (MPa)	G_2 (MPa)	τ_{max} (MPa)	γ_{max}
SL-0.01- 1,2,3	0.01	0.007	22.8 ± 0.6	0.19 ± 0.01	3.4 ± 0.1	1.9 ± 0.0	7.4 ± 0.4	2.4 ± 0
SL-0.05- 1,2,3	0.05	0.033	26.9 ± 2.1	0.22 ± 0.01	5.0 ± 0.3	1.7 ± 0.2	8.9 ± 0.2	2.3 ± 0
SL-0.1- 1,2,3	0.1	0.066	29.1 ± 0.9	0.23 ± 0.01	5.3 ± 0.4	1.6 ± 0.1	9.3 ± 0.3	2.3 ± 0.2
SL-0.5- 1,2,3	0.5	0.330	30.3 ± 1.2	0.27 ± 0.01	6.6 ± 0.4	1.5 ± 0.1	9.4 ± 0.8	2 ± 0.3
SL-1.0- 1,2,3	1.0	0.660	32.2 ± 1.0	0.28 ± 0.01	8.1 ± 0.4	1.5 ± 0.0	10.5 ± 0.4	1.7 ± 0.1
SL-5.0- 1,2,3	5.0	3.300	33.1 ± 1.7	0.31 ± 0.01	9.7 ± 0.9	1.4 ± 0.2	11.9 ± 0.7	1.6 ± 0.1

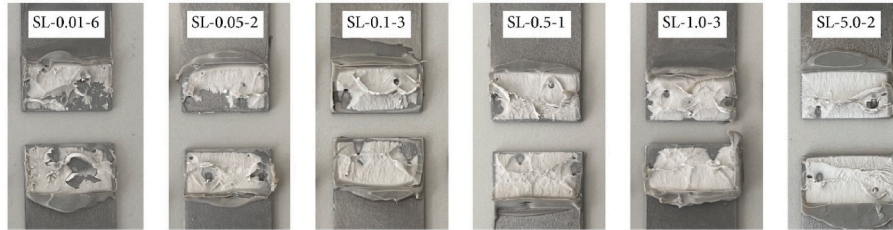


Fig. 6. Cohesive failure of single-lap specimens under various applied displacement rates.

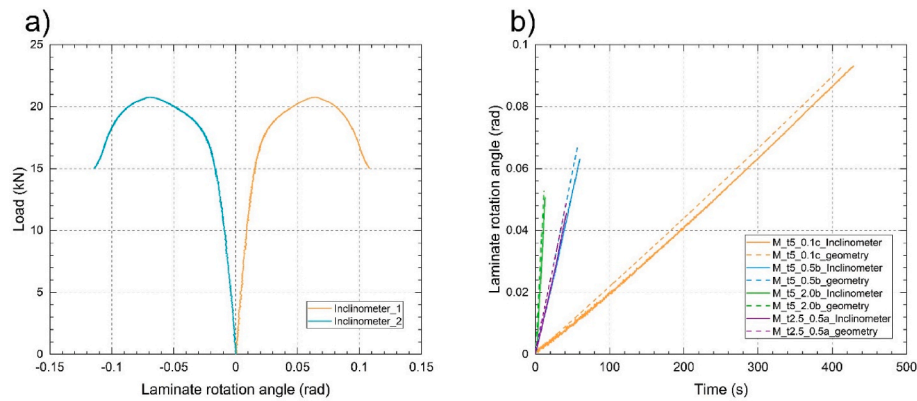


Fig. 7. Inclinator data: a) Comparing two inclinometers against machine load for specimen M-t5-0.1b; b) Comparing inclinometer data with geometrically calculated rotations over time for specimens M-t5-0.1b, M-t5-0.5b, M-t5-2.0b, M-t2.5-0.5a.

2.5.2.2. Torsion-rotation curve analysis. The torsional moment-laminate rotation responses of the angle joints subjected to monotonic loading are presented in Fig. 8. The torsional responses were calculated using Eq. (3), considering the loads measured by the machine. The laminate rotation angles presented in Fig. 8 were calculated using Eq. (8). Fig. 8 (a) illustrates the torsion-laminate rotation responses for specimens with

a 5 mm adhesive layer thickness, whereas Fig. 8(b) shows the results for specimens subjected to an applied displacement rate of 0.5 mm/s, with adhesive layer thicknesses of 5 mm and 2.5 mm. The torsion-rotation responses of the angle joint specimens can be described by the following two distinct phases: (a) the initial linear segment until the onset of yielding of the joint area, and (b) the continuous decrease in

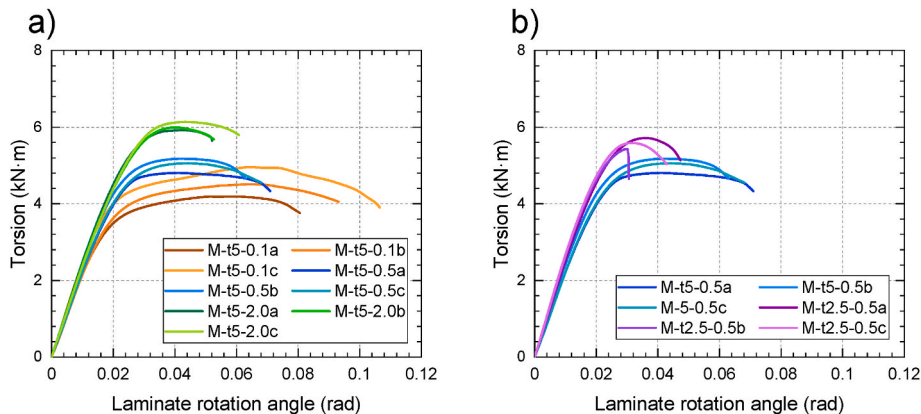


Fig. 8. Angle joint torsion-rotation relation a) for specimens with 5 mm adhesive layer thickness subjected to various applied displacement rates, b) for specimens with 5 mm and 2.5 mm adhesive layer thickness subjected to 0.5 mm/s applied displacement rate.

tangential stiffness until the maximum torsional capacity is reached. The stage (a) is characterized by two parameters, the slope of the initial linear segment, S , and the laminate rotation angle at the onset of yielding in the joint area, θ_y . Meanwhile, the stage (b) is characterized by two parameters, the maximum torsional moment, T_{\max} , and the laminate rotation angle at maximum torsion, θ_{\max} . With the increase of the applied displacement rate, S , θ_y , and T_{\max} , increased while θ_{\max} decreased. At the highest displacement rate, T_{\max} attained its maximum value, in contrast to θ_{\max} , which was the highest at the lowest rate. Compared to the specimens with a 5.0 mm adhesive layer, those with a thinner 2.5 mm adhesive layer thickness exhibited a higher initial stiffness and maximum torsional moment, by 15% and 11%, respectively. However, this reduction in thickness led to a 40% decrease in θ_{\max} . Table 2 provides a summary of $\dot{\theta}$, S , θ_y , T_{\max} , and θ_{\max} values for each specimen.

2.5.2.3. - Shear strain variation. The shear strain at a particular point in the joint area, having a rotational deformation of $2 \times \theta$ about its centroid (Fig. 9(a)), can be calculated using the following relationship:

$$\gamma = \frac{r \times 2 \times \theta}{t_a} \quad \text{Eq. (9)}$$

where r denotes the distance from the point of interest to the center of rotation, and t_a is the adhesive thickness. The shear strain is thus constant through the thickness, as shown in Fig. 9(b), and the shear stress distribution is uniform through the thickness at a particular point in the joint area (Fig. 9(c)).

Fig. 10 displays the images of M-t5-0.1c joint along its outer and inner edges. Fig. 10(a) and (b) are at the beginning and end of stage (a), when the specimen is at its undeformed state and onset of yield, respectively. Fig. 10(c) corresponds to the end of stage (b), with maximum achieved torsion, while Fig. 10(d) displays the state at which the torsion was dropped to 80% of its maximum value. For each pair of images, the left one was captured by the DIC system, whereas the right one was taken with a digital camera to track the propagation of failure along the back-facing edges. In Fig. 10(b), no failure is apparent in the joint at the onset of yielding. Meanwhile, Fig. 10(c) shows cracks initiating at the corners and propagating towards the middle of the edge at maximum torsion. Finally, Fig. 10(d) illustrates the final state of the specimens, showing the detached adhesive layer at the edges from laminates on both sides, which propagates towards the center of the joint area with further applied deformation. The 3D DIC measurements showed no relative displacements between the laminates up to the maximum torsion; bolt bearing failure in the inner laminate did thus not yet initiate.

Shear strain distributions in the adhesive layer along the edge of the joint area can be calculated using the DIC recordings. The origin of the DIC recorded coordinates was assumed to be on the top face of an outer laminate at the center point of the joint area with X, Y, and Z axes pointing in the joint thickness, vertical, and horizontal directions,

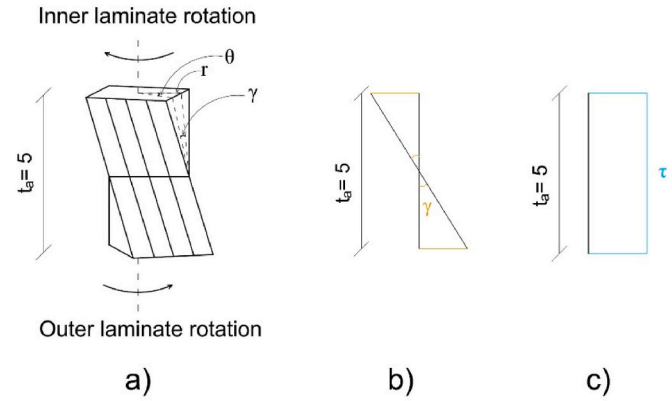


Fig. 9. a) Schematic representation of deformed adhesive layer subjected to opposite rotation of inner and outer laminates, b) corresponding constant shear strain, c) corresponding uniform shear stress across adhesive thickness.

respectively, as shown in Fig. 10(a). The shear strain for a specific point over the recorded area can be calculated from the DIC data as follows:

$$\gamma_{DIC} = \frac{\sqrt{(y_t - y_0)^2 + (z_t - z_0)^2}}{|x_0 - x_m|} \quad \text{Eq. (10)}$$

where x , y , and z represent the coordinates of a certain point either at the start (undeformed state), x_0 , y_0 , and z_0 , or at a given time of t (deformed state), y_t and z_t . The value of x_m , the x coordinate at the mid-thickness of the adhesive layer, depends on the adhesive layer. Specifically, x_m is -12.5 mm for the adhesive layer with x between -10 mm and -15 mm, and -27.5 mm for the one with x between -25 mm and -30 mm. Fig. 11 (a) and (b) present the γ values calculated along the captured edge of the adhesive layer from the recorded DIC coordinates at ten intervals at stages (a) and (b), as explained previously, for the M-t5-0.1c and M-t5-0.5b joints, respectively. Shear strain values along the captured edge ($y = -50$ mm– 50 mm at $z = -50$ mm) were also calculated using Eq. (9) with r values between 50 mm and 70.7 mm, corresponding to the distance from the edge of the adhesive layer to the joint centroid, and the corresponding rotation, and depicted in Fig. 11 as dashed lines. As shown in Fig. 11, the values obtained from Eq. (9) are in good agreement with DIC results. Yield shear strains at the corners, γ_y , were determined to be 0.32 and 0.38 for M-t5-0.1c and M-t5-0.5b joints, respectively. The maximum shear strain at the corner, γ_{\max} , was found to be 1.51 and 1.12 for M-t5-0.1c and M-t5-0.5b joints. The corner points at the adhesive layer edge corresponding to stage (b) in Fig. 11 were eliminated from the curve due to the formation of small cracks.

Similar to the shear strain relation (Eq. (9)), the shear strain rate, $\dot{\gamma}$, can be calculated at each point as follows:

$$\dot{\gamma} = \frac{r \times 2 \times \dot{\theta}}{t_a} \quad \text{Eq. 11}$$

where $\dot{\theta}$ is reported in Table 2 for each displacement rate. Fig. 12(a)–(d) illustrate the linear variation of $\dot{\gamma}$ for specimens with 5 mm adhesive layer thickness under laminate rotation rates of 0.0002 , 0.0011 , and 0.0044 rad/s and specimen with 2.5 mm adhesive layer thickness under laminate rotation rate of 0.0011 rad/s, respectively. Strain rate values are shown along two axes, one passing through the middle of the edges and the other passing through the corners. The strain rate value at the middle of the edge and the corner are denoted as $\dot{\gamma}_m$ and $\dot{\gamma}_c$, respectively.

2.5.2.4. Failure mode. Fig. 13(a)–(c) illustrate the failure surfaces of the inner and outer laminates of angle joints with 5 mm adhesive thickness subjected to three different laminate rotation rates of 0.00022 , 0.0011 , and 0.0044 rad/s, respectively. Meanwhile, Fig. 13(d) shows the failure surface of an angle joint with 2.5 mm adhesive thickness under a

Table 2
Angle joint experimental results.

Sp. name	$\dot{\theta}$ (rad/s)	S (kN-m/rad)	θ_y (rad)	T_{\max} (kN-m)	θ_{\max} (rad)
M-t5-0.1a	0.0002	221.4	0.010	4.19	0.060
M-t5-0.1b	0.0002	223.6	0.010	4.51	0.066
M-t5-0.1c	0.0002	250.9	0.011	4.96	0.065
M-t5-0.5a	0.0011	229.4	0.012	4.81	0.041
M-t5-0.5b	0.0011	250.4	0.013	5.17	0.043
M-t5-0.5c	0.0011	228.7	0.012	5.06	0.045
M-t5-2.0a	0.0044	250.4	0.015	5.92	0.044
M-t5-2.0b	0.0044	244.1	0.014	5.99	0.041
M-t5-2.0c	0.0044	240.2	0.014	6.13	0.043
M-t2.5-0.5a	0.0011	256.0	0.013	5.71	0.036
M-t2.5-0.5b	0.0011	271.7	0.013	5.43	0.030
M-t2.5-0.5c	0.0011	274.6	0.014	5.59	0.032

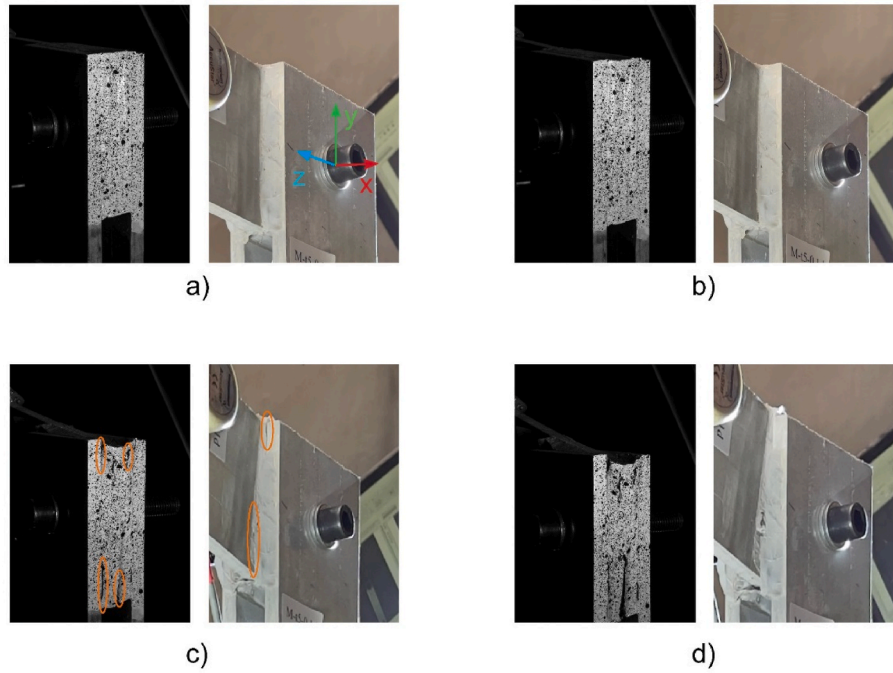


Fig. 10. DIC and tracking camera captured photos of specimen M-t5-0.1c at a) onset of experiment, b) onset of yielding, c) maximum torsion, and d) when torsion drops to 80% of maximum torsion.

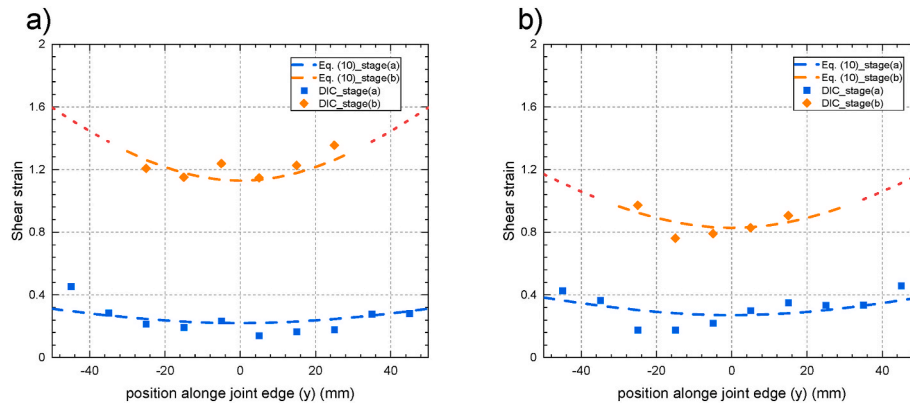


Fig. 11. Shear strain variation obtained from DIC data along the joint edge at end of stages (a) and (b) of torsion-rotation behavior at $x = 10$ for a) M-t5-0.1c and b) M-t5-0.5b.

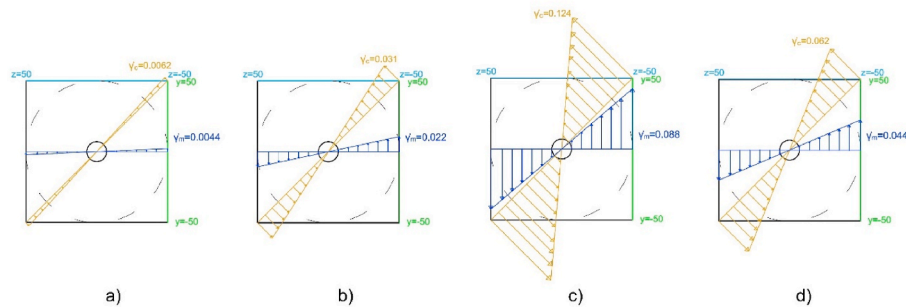


Fig. 12. Shear strain rate distribution of a) M-t5-0.1 b) M-t5-0.5, c) M-t5-2.0, and d) M-t2.5-0.5.

laminate rotation rate of 0.0011 rad/s. Five different failure modes were observed: cohesive failure, C, fiber tear, F, shear-out, S, net tension, N, and adhesive interface failure, A, each specified by a dashed line or an ellipse in Fig. 13. The adhesive interface failure precedes all other failure

modes, initiating in the corners of the joint area and continuing up to the ultimate failure of the specimen. No evidence of shear-out or net tension failure modes was observed during the experiments up to stage (b) of the torsion-rotation behavior of the specimens. Shear-out and net tension

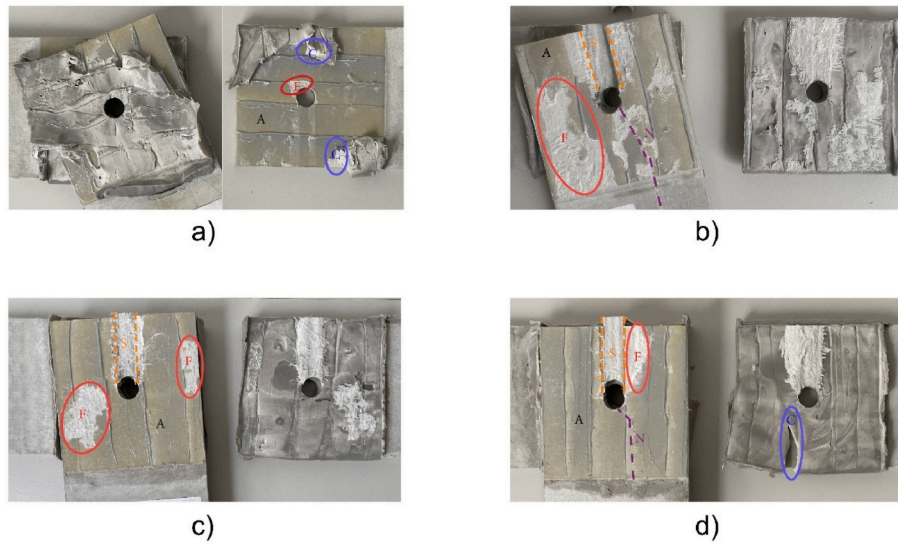


Fig. 13. Combination of failure modes for angle-joints under a) 0.00022 rad/s (M-t5-0.1b) b) 0.0011 rad/s (M-t5-0.5a) c) 0.0044 rad/s (M-t5-2.0b) d) 0.0011 rad/s (M-t2.5-0.5a) laminate rotation rates, C = cohesive, F = fiber tear, S = shear-out, and N = net tension, A = adhesive/interface.

failure modes occurred only after further application of the displacement beyond stage (b). Cohesive failure was mostly observed in angle joints subjected to the lowest applied laminate rotation of 0.00022 rad/s while being only slightly observed in angle joints with a 2.5 mm adhesive layer thickness subjected to the laminate rotation of 0.0011 rad/s. In all other cases, fiber tear failure was observed, followed by shear-out and net tension failure modes after reaching maximum joint capacity.

3. Analytical model

An analytical model was developed to predict the behavior of the pseudo-ductile adhesive angle joints torsion-rotation response, considering the rate-dependent characteristics of the pseudo-ductile adhesive. This approach was selected since each point within the adhesive layer of the angle joint experiences a different strain rate relative to its distance from the center of rotation making it challenging to calculate the shear stress distribution using conventional methods (Eq. (4) and (5)).

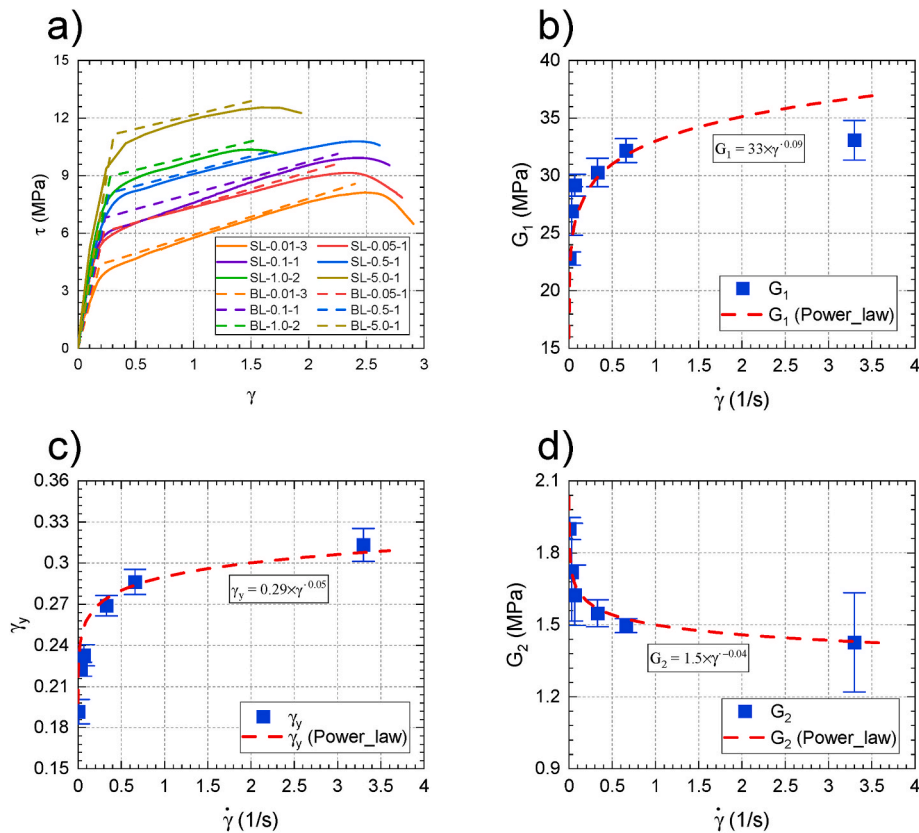


Fig. 14. Comparison of single-lap joint stress-strain responses between experimental results and bilinear model.

The initial step in developing the torsional behavior model involved fitting a bilinear model to the single-lap joint experimental results obtained under six distinct shear strain rates (mentioned in Section 2.5.1 and Table 1). The bilinear model comprises a pre-yield section with two parameters of G_1 and γ_y , and a post-yield section with two parameters of G_2 and γ_{\max} . A power-law relationship was then fitted to G_1 , γ_y , and G_2 parameters, and the corresponding shear strain rate. The power-law relations between the pseudo-ductile adhesive bilinear model parameters and the shear strain rate under the aforementioned laboratory condition of the single-lap joints are expressed as follows:

$$G_1 = 33 \times \dot{\gamma}^{0.09} \quad \text{Eq. 12}$$

$$\gamma_y = 0.29 \times \dot{\gamma}^{0.05} \quad \text{Eq. 13}$$

$$G_2 = 1.5 \times \dot{\gamma}^{-0.04} \quad \text{Eq. 14}$$

Fig. 14(a) presents the experimental results (dashed lines) and their corresponding bilinear model (solid lines), while Fig. 14(b)–(c) show the fitted power-law relations to G_1 , γ_y , and G_2 data, previously reported in Table 1.

Since the failure mode of the single-lap joints was different from that of the angle joints, γ_{\max} values were obtained from angle joint experiments and then denominated as $\gamma_{\max, \text{angle}}$. To estimate the values of $\gamma_{\max, \text{angle}}$ a power-law relation was fitted to the maximum shear strain over the results of angle joint experiments obtained from the DIC data. The resulting power-law relation is as follows:

$$\gamma_{\max, \text{angle}} = 0.7 \times \dot{\gamma}^{-0.14} \quad \text{Eq. 15}$$

In the next step, the torsion moment within the adhesive layer, T , can be calculated by integrating torsion moment increments as follows:

$$T = \int_{-50}^{50} \int_{-50}^{50} r \times \tau \times dydz \quad \text{Eq. 16}$$

where $dy \cdot dz$ is the area increment at each point of the joint area, with y and z ranging from -50 to 50 considering the origin at the center of the middle bolt in Fig. 10(a), τ is the shear stress at the corresponding area increment, and r is the length of the arm from the joint center (center of rotation) for a point with y and z coordinates which can be determined as follows:

$$r = \sqrt{y^2 + z^2} \quad \text{Eq. 17}$$

The stress at each point was derived based on the bilinear model by applying the following conditions:

$$\tau = G_1 \times \gamma \quad \text{if } \gamma \leq \gamma_y \quad \text{Eq. 18}$$

$$\tau = G_1 \times \gamma_y + G_2 \times (\gamma - \gamma_y) \quad \text{if } \gamma_y < \gamma \leq \gamma_{\max, \text{angle}} \quad \text{Eq. 19}$$

$$\tau = 0 \quad \text{if } \gamma_{\max, \text{angle}} < \gamma \quad \text{Eq. 20}$$

Using the described procedure for each rotation angle of the laminates, θ , the torsion-rotation response of the angle joint can be predicted.

Fig. 15 presents the experimental results of angle joints (dashed lines) and the predicted torsion-rotation response (solid lines). Fig. 15 (a)–(c) depict these responses for the specimens with an adhesive layer thickness of 5 mm subjected to laminate rotation rates of 0.00022, 0.0011, and 0.0044 rad/s, respectively. Meanwhile, Fig. 15(d) shows the aforementioned responses and predictions for the specimens with an adhesive layer thickness of 2.5 mm under a laminate rotation rate of 0.0011 rad/s.

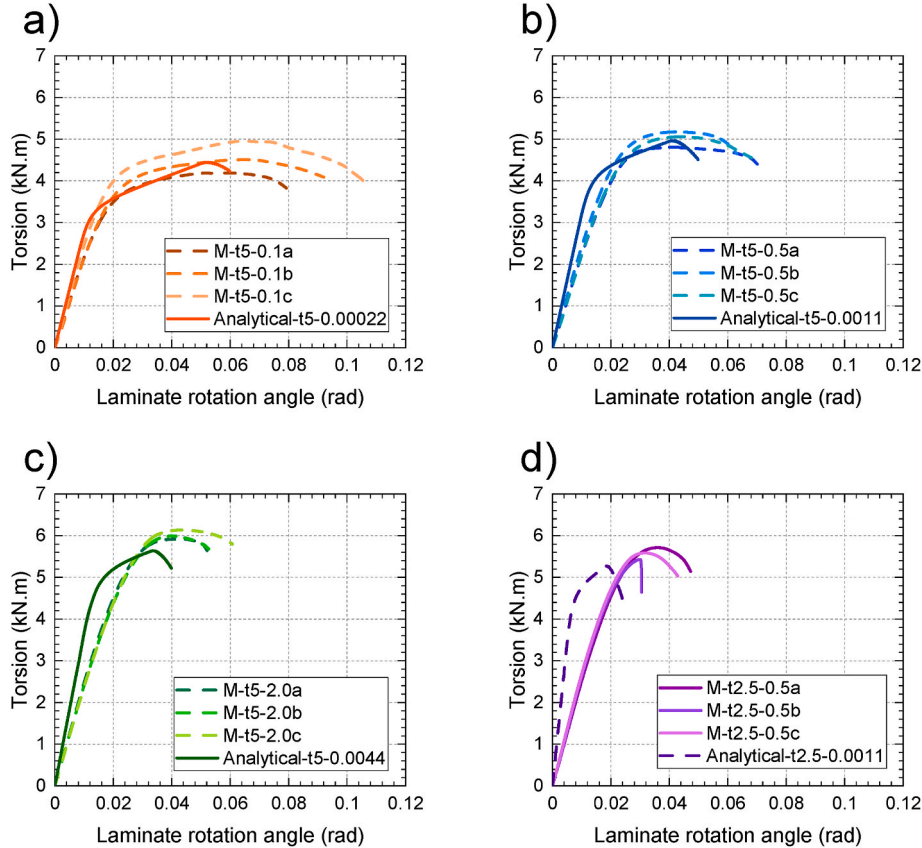


Fig. 15. Torsion-rotation response comparison of experimental and analytical results for specimens a) M-t5-0.1, $\dot{\theta} = 0.00022 \text{ rad/s}$, b) M-t5-0.5, $\dot{\theta} = 0.0011 \text{ rad/s}$, c) M-t5-2.0, $\dot{\theta} = 0.0044 \text{ rad/s}$, and d) M-t2.5-0.5, $\dot{\theta} = 0.0011 \text{ rad/s}$.

4. Discussion

4.1. Analytical model validation and discussion

As it is shown in Fig. 5(b), in single-lap joints under tension, the pseudo-ductile adhesive exhibited a uniform shear strain distribution across the joint area. In contrast, in angle joints subjected to torsion, the shear strain distribution is not uniform as it changes depending on the distance from the center of rotation over the joint area of the adhesive layer, as it is shown in Fig. 11.

The comparison between experimental results of angle joints and the predicted torsion-rotation response for the specimens under different laminate rotation rates, $\dot{\theta}$, and different adhesive layer thicknesses are presented in Fig. 15. A good agreement between the analytical model predictions and experimental results is observed, especially for the lower laminate rotation rates (Fig. 15 (a) and (b)). However, the analytical model and experimental results do not exhibit good agreement at higher strain rates during the pre-yield stage. This discrepancy may be attributed to the basis of the analytical model, in which the stress-strain relationship was obtained from a uniform strain rate distribution. The analytical model, however, demonstrates robust validation for the post-yield stage, with the maximum torsion being of higher importance in the joint design process.

By using the developed analytical model, the stress distribution profile across the joint area in each angle joint specimen can be derived. Fig. 16 illustrates the predicted shear stress profile along two axes passing through either the corners or the middle of the edge of the joint area. The stress profiles are depicted at the yield and maximum stages, stage (a) and stage (b), respectively, for a specimen with an adhesive layer thickness of 5 mm subjected to a 0.0044 rad/s laminate rotation rate. The figure highlights the fact that the points lying on a circle at a distance r from the joint centroid have identical shear stress values. The corner stress, τ_c , was calculated to be equal to 7.2 MPa at stage (a) and increased to 8.2 MPa up to stage (b). The shear stress at the middle of the edge, τ_m , rises from 5.0 MPa to 7.5 MPa from stage (a) up to its maximum (stage (b)). The slight difference between the maximum shear stress at the corners and the middle of the edge can be attributed to the lower shear strain rate at the middle of the edge. This emphasizes the rate-dependent nature of the adhesive and its impact on shear stress distribution within the joint area under torsional loading.

Fig. 17 displays the radial shear stress profiles for r values ranging from 7 to 70.7 mm at the stage where the whole joint area is in the pre-yield state, end of stage (a), and the state at which the maximum torsion is achieved, end of stage (b). Each case comprises four curves representing: three angle joints with an adhesive layer thickness of 5 mm under laminate rotation of 0.00022, 0.0011, 0.0044 rad/s, and an angle joint with an adhesive layer thickness of 2.5 mm subjected to a 0.0011 rad/s laminate rotation rate. For each specimen, the corresponding

rotation angles at which the corner of the joint area reaches its yield and maximum strength, obtained from the analytical model, are reported in the legends of Fig. 17(a) and (b), respectively. In Fig. 17(a) each stress profile shows a slightly convex (upward) curvature since the power-law relations of the two pre-yield bilinear model parameters are increasing with the strain rate. In Fig. 17(b) the shear stresses at $r = 70.7$ dropped to zero, due to reaching maximum strain at the corners. A significant decrease in the slope of each stress profile in Fig. 17(b) indicates the distance, r , beyond which the points are in the post-yield region of the bilinear behavior, whereas the points with a smaller r , are in the pre-yield state. At the end of stage (b), 3% of the joint area ($r < 10$ mm) for specimens subjected to 0.00022 rad/s and 10% of the joint area ($r < 18$ mm) for specimens under 0.0044 rad/s are still in their pre-yield state. The slightly concave (downward) curvature in the post-yield section of the stress profiles in Fig. 17(b) was caused by the decreasing power-law relations of the two bilinear model post-yield parameters with the strain rate.

The shear stress-strain relationship at the middle point of the edges of the specimens under different laminate rotation rates and adhesive thicknesses with $\dot{\gamma}_m$ of 0.0044, 0.022, 0.088, and 0.044 1/s, displayed in Fig. 12, are shown in Fig. 18 throughout the experiment. As shown in this figure, the shear stress-strain curve corresponding to the specimen with adhesive thickness of 2.5 mm under 0.0011 rad/s laminate rotation rate falls between those of the specimens with a thickness of 5 mm subjected to 0.0011 and 0.0044 rad/s laminate rotation rates, following the magnitude of their shear strain rate.

The shear strain rate at the mid-edge of the joint area, $\dot{\gamma}_m$, was considered as the representative strain rate for each specimen to investigate further the strain rate effects in the following sections.

4.2. Variable strain rate effect

To elucidate the effects of strain rate on the torsion-rotation behavior of the angle joints, the average values and corresponding standard errors of S , θ_y , T_{max} , and θ_{max} , were computed for specimens with the same adhesive thickness and under the same laminate rotation rate. These extracted parameters were subsequently plotted against the strain rate, as illustrated in Fig. 19(a)-(d), respectively. The analytical bilinear model results are also represented in Fig. 19 with a solid line.

An increase in the strain rate resulted in an increase in initial stiffness, yield rotation, and maximum torsional moment, but caused a decrease in maximum rotation. The predicted analytical response overestimated the initial stiffness and underestimated the yield rotation of the experimental data with the difference increasing with the strain rate. However, the predicted analytical response was in good agreement with the experimental data for the maximum torsion and rotation.

With the increase in strain rate, the molecular chains of the pseudo-ductile adhesive have less time to uncoil and rearrange to the applied

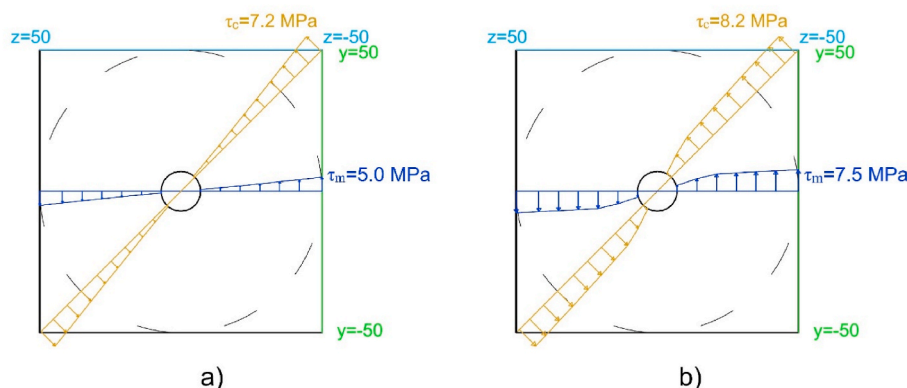


Fig. 16. Shear stress distribution for M-t5-2.0 with $\dot{\theta} = 0.0044$ at a) stage (a) and b) stage (b).

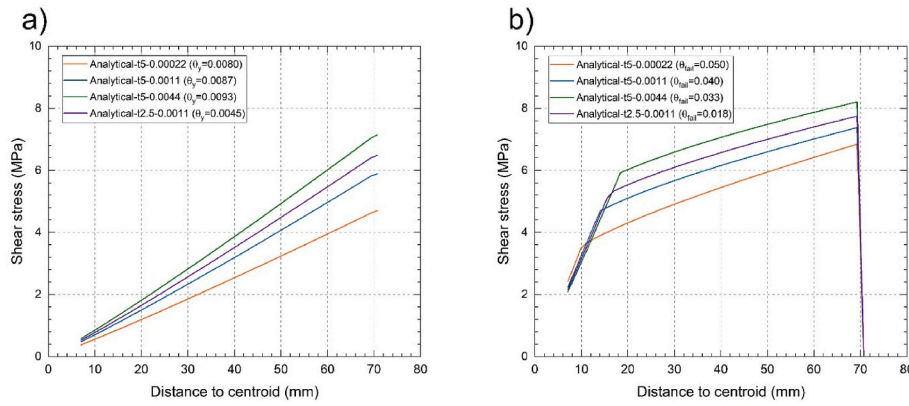


Fig. 17. Shear stress distribution in radial direction of specimens under different laminate rotation rate and adhesive thickness at end of a) stage (a) and b) stage (b).

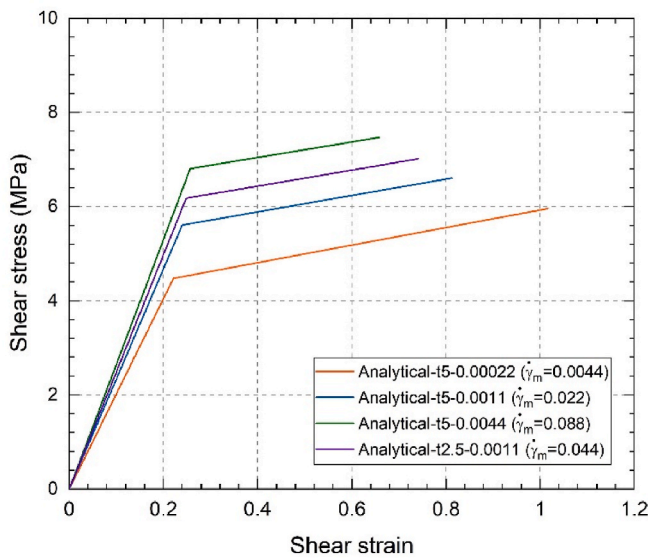


Fig. 18. Estimated bilinear shear stress-strain at middle point of edges of specimens under different laminate rotation rate and adhesive thickness during experiment.

load direction. This phenomenon contributes to the higher stiffness within the pre-yield linear region as represented by both the experimental and analytical results in Fig. 19(a). The experimental data shows an increase in the initial stiffness by 5% (from 232 to 245 MPa) as the strain rate increases, while the analytical results show a more pronounced 32% increase (from 276 to 365 MPa). The overestimation of the initial stiffness in the torsion-rotation response in the analytical results arises from the incorporated stress-strain relationship from the single-lap joint experimental results with uniform stress distribution.

The stiffer response at higher strain rates leads to an increase in both yield rotation and maximum torsion and a decrease in rotation at the maximum torsion as presented in Fig. 19(b)–(d), respectively. In Fig. 19(b) the analytical results demonstrate a 22% underestimation compared to the experimental results at lower strain rates, and a more pronounced underestimation of 38% at higher strain rates. This underestimation of the yield rotation can be attributed to the same reason as for initial stiffness. However, the analytical results for maximum torsion and rotation at the maximum torsion, as illustrated in Fig. 19(c) and (d), respectively, are in good agreement with the experimental results in both values and trends.

4.3. Effect of adhesive layer thickness

Both angle joint specimens of M-t5-0.5 and M-t2.5-0.5 with respective adhesive layer thicknesses of 5 and 2.5 mm were experimented under the same laminate rotation rate of 0.0011 rad/s. By decreasing the adhesive layer thickness, the shear strain rate range expanded from 0 to 0.031 to 0–0.062, consequently leading to a rise in initial stiffness and yield rotation followed by enhanced strength, as depicted in Fig. 19(a)–(c). Conversely, the maximum rotation experienced a decrease, as illustrated in Fig. 19(d). These trends are in line with the overall trends of S , θ_y , T_{max} , and θ_{max} for specimens with 5 mm adhesive thickness versus strain rate. The analytical model is also capable of predicting the trend of the variables for the thinner adhesive thickness.

4.4. Effect of adhesive joint type on ductility

In this section, the stress-strain responses from the linear single-lap joints and torsion-rotation responses of the angle joint are compared with the load-displacement behavior of linear double-lap joints with the same materials and adhesive joint area as the angle joints, according to the results presented in a previous research [32].

Fig. 20(a) provides insight into the effect of strain rate on the ductility of the studied adhesive joint types. The ratio of the area under the post-yield segment of their respective stress-strain, torsion-rotation, or load-displacement curves (i.e., the dissipated inelastic energy), to their total area (i.e., total energy = elastic energy + inelastic energy) [33], ductility ratio, is used to quantify the pseudo-ductility of the adhesive joints. The results show that the ductility ratio, μ , is higher for lower strain rates and decreases with strain rate for all three adhesive joint types (note $\mu = 1.0$ denotes full ductility, neglecting the elastic segment). This behavior is expected for pseudo-ductile adhesives, as higher strain rates result in a more brittle response due to the reduced time available for deformation and energy dissipation. Furthermore, it can be observed that the ductility ratio varies among the different experiment types. Both the linear double-lap and the linear single-lap joints demonstrate a higher ductility ratio compared to the angle joint, particularly at the lowest strain rate. This difference can be attributed to the uniform strain rate distribution of the linear double-lap and linear single-lap joints, contrasted with the nonuniform strain rate distribution observed in the angle joints. The almost overlapping results of the linear lap joints also demonstrate that, due to the uniform strain rate distributions, the ductility becomes independent of scale, i.e. $13 \times 25.0 \times 1.5$ mm versus $100 \times 100 \times 5$ mm adhesive layer geometries.

Fig. 20(b) shows the pre-yield to post-yield stiffness ratio versus strain rate. This ratio is always higher than one due to the inherently higher stiffness in the pre-yield stage. The results show that the ratio increases with increasing strain rate for all three adhesive joints, consistent with the previously explained behavior of pseudo-ductile

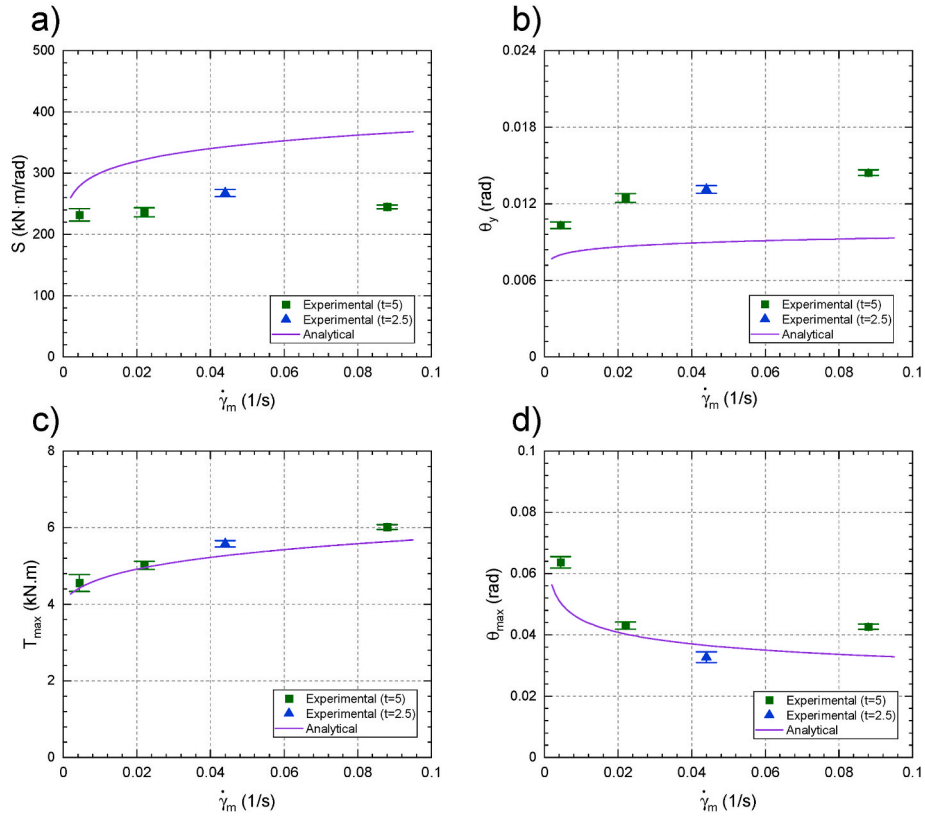


Fig. 19. Variation of parameters a) S , b) θ_y , c) T_{\max} , and d) θ_{\max} versus effective strain rate.

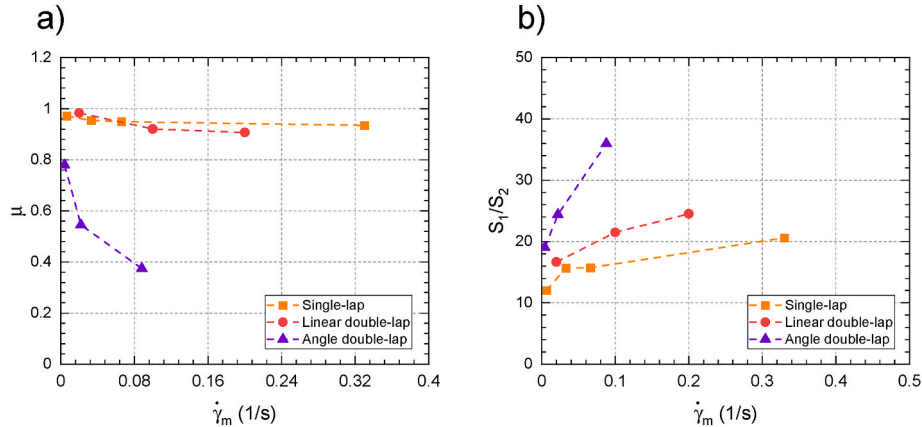


Fig. 20. Comparison of three adhesive joint experiments for a) inelastic energy to total energy ratio, b) pre-yield stiffness to post-yield stiffness ratio, vs. strain rate.

adhesives (Fig. 14(d)). This behavior results from the slower increase in deformation at lower strain rates, leading to lower pre-yield stiffness, and then allowing the molecular chains to be aligned in the applied deformation direction, leading to a stiffening effect in the post-yield stage. Furthermore, the ratio varies across the joint types. The angle joint exhibits the highest ratio across all strain rates, indicating its inability to effectively exploit the stiffening advantage of the pseudo-ductile adhesives due to the variable strain rate in the adhesive layer. In the adhesive layer, regions close to the center of rotation exhibit lower shear strain and strain rate, consequently remaining in the pre-yield stage characterized by coiled molecular chains. As the distance from the rotation center increases, the molecular chains are subjected to increasing shear strains and strain rates, which enables their uncoiling and reorientation in the tangential direction. However, in the regions furthest from the center of rotation, the molecular chains, which are in

the post-yield stage, do not have sufficient time to fully uncoil and reorient tangentially before the failure of the joint. This partially rearranged molecular chain structure in the adhesive layer results in a diminished stiffening effect and reduced stiffness after yielding. Consequently, the adhesive layer fails at its interface specially under the highest laminate rotation rate when the joint area experienced the largest range of the strain rate as indicated in Fig. 13.

5. Conclusions

A novel bonded-bolted angle joint incorporating a central bolt that constrains relative translational deformation but allows for rotational deformation in the adherend plane was developed in this study. Pure torsion moments are imposed in the adhesive layers in this configuration, causing the formation of variable strain rates in the joint in the

radial direction from the rotation center. Accordingly, the static behavior of the hybrid bonded-bolted angle joints was investigated, focusing on the effects of induced variable strain rates, adhesive thickness, and adhesive joint type. The results provide insights into the complex performance characteristics of adhesive joints, particularly under variable strain rates. The conclusions from this experimental and analytical investigation are as follows.

- 1 The angle joint experimental results showed nonuniform shear strain distribution in the radial direction from the rotation center, induced by torsion, in contrast to the single-lap joint experiments.
- 2 The initial stiffness, yield rotation, and maximum torsion, of the angle-joint experimental results showed increasing trends with the strain rate, while the maximum rotation showed a decreasing trend, all aligned with the rate-dependent molecular chain movement of the pseudo-ductile adhesive.
- 3 The analytical model developed using the stress-strain relation from single-lap joints with uniform stress distribution overestimated the initial stiffness of the angle joint results with nonuniform stress distribution. However, it could provide good estimations for the strength and post-yield behavior.
- 4 The angle joint with a thinner adhesive layer exhibited a higher initial stiffness and increased strength in torsion-rotation behavior due to a higher shear strain rate.
- 5 The adhesive joint ductility is influenced by both strain rate and joint configuration. Lower strain rates enhance ductility in pseudo-ductile adhesives in all joint configurations. Meanwhile, the lower ductility observed in angle joints compared to linear double-lap and single-lap joints shows that the pseudo-ductile adhesive capacity may not be fully utilized in the angle configuration, due to the nonuniform strain rate in the radial direction from the rotation center of the adhesive layers.
- 6 The angle joints exhibited the highest pre-yield stiffness to post-yield stiffness ratio across all strain rates, indicating that they cannot effectively exploit the stiffening advantage of the pseudo-ductile adhesive.

6. Authorship contribution statement

Ghazaleh Eslami: Conceptualization, Investigation, Experimentation, Formal Analysis, Concept Development, Prediction, Writing - original draft, Writing - review & editing.

A.Vahid Movahedirad: Validation, Writing - review & editing.

Thomas Keller: Conceptualization, Validation, Writing - review & editing, Supervision.

Declaration of competing interest

The authors declare that they have no known competing financial interests or personal relationships that could have appeared to influence the work reported in this paper.

Data availability

The data that has been used is confidential.

Acknowledgements

The authors express their sincere appreciation to Sika AG, Switzerland, for supplying the adhesive, and Fiberline Composites A/S, Denmark, for providing the pultruded laminates used in this research.

References

- [1] Vedernikov A, Safonov A, Tucci F, Carlone P, Akhatov I. Pultruded materials and structures: a review. *J Compos Mater* 2020. <https://doi.org/10.1177/0021998320922894>.
- [2] Xin H, Liu Y, Mosallam AS, He J, Du A. Evaluation on material behaviors of pultruded glass fiber reinforced polymer (GFRP) laminates. *Compos Struct* 2017;182:283–300. <https://doi.org/10.1016/j.compstruct.2017.09.006>.
- [3] Bank LC. Progressive failure and ductility of FRP composites for construction: review. *J Compos Construct* 2013;17:406–19. [https://doi.org/10.1061/\(asce\)cc.1943-5614.0000355](https://doi.org/10.1061/(asce)cc.1943-5614.0000355).
- [4] Feng P, Wu Y, Ding Y, Liu TQ, Tian Y. Quasi-plastic flexural behavior of adhesive-bolt hybrid connection for large scale pultruded GFRP frame. *Eng Struct* 2021;238:112200. <https://doi.org/10.1016/j.engstruct.2021.112200>.
- [5] de Castro J, Keller T. Design of robust and ductile FRP structures incorporating ductile adhesive joints. *Composites Part B* 2010;41:148–56. <https://doi.org/10.1016/j.compositesb.2009.10.003>.
- [6] Keller T, De Castro J. System ductility and redundancy of FRP beam structures with ductile adhesive joints. *Composites Part B* 2005;36:586–96. <https://doi.org/10.1016/j.compositesb.2005.05.001>.
- [7] Bank LC, Mosallam AS, McCoy GT. Design and performance of connections for pultruded frame structures. *J Reinforc Plast Compos* 1994;13:199–212. <https://doi.org/10.1177/073168449401300302>.
- [8] Bank LC, Yin J, Moore L, Evans DJ, Allison RW. Experimental and numerical evaluation of beam-to-column connections for pultruded structures. *J Reinforc Plast Compos* 1996;15:1052–67. <https://doi.org/10.1177/073168449601501005>.
- [9] Smith SJ, Parsons ID, Hjelmstad KD. An experimental study of the behavior of connections for pultruded GFRP I-beams and rectangular tubes. *Compos Struct* 1998;42:281–90. [https://doi.org/10.1016/S0263-8223\(98\)00082-8](https://doi.org/10.1016/S0263-8223(98)00082-8).
- [10] Carrion JE, LaFave JM, Hjelmstad KD. Experimental behavior of monolithic composite cuff connections for fiber reinforced plastic box sections. *Compos Struct* 2005;67:333–45. <https://doi.org/10.1016/j.compstruct.2004.01.015>.
- [11] Ascione F, Lamberti M, Razaqpur AG, Spadea S. Strength and stiffness of adhesively bonded GFRP beam-column moment resisting connections. *Compos Struct* 2017;160:1248–57. <https://doi.org/10.1016/j.compstruct.2016.11.021>.
- [12] Ascione F, Lamberti M, Razaqpur AG, Spadea S, Malagie M. Pseudo-ductile failure of adhesively joined GFRP beam-column connections: an experimental and numerical investigation. *Compos Struct* 2018;200:864–73. <https://doi.org/10.1016/j.compstruct.2018.05.104>.
- [13] Mottram JT, Zheng Y. State-of-the-art review on the design of beam-to-column connections for pultruded frames. *Compos Struct* 1996;35:387–401. [https://doi.org/10.1016/S0263-8223\(96\)00052-9](https://doi.org/10.1016/S0263-8223(96)00052-9).
- [14] Qureshi J, Nadir Y, John SK. Bolted and bonded FRP beam-column joints with semi-rigid end conditions. *Compos Struct* 2020;247:112500. <https://doi.org/10.1016/j.compstruct.2020.112500>.
- [15] Ascione F, Granata L, Carozzi G. Flexural and shear behaviour of adhesive connections for large scale GFRP frames: influence of the bonded area and hygro-thermal aging. *Compos Struct* 2022;283:115122. <https://doi.org/10.1016/j.compstruct.2021.115122>.
- [16] Girão Coelho AM, Mottram JT. A review of the behaviour and analysis of bolted connections and joints in pultruded fibre reinforced polymers. *Mater Des* 2015;74:86–107. <https://doi.org/10.1016/j.matdes.2015.02.011>.
- [17] EN 1998-1. Eurocode 8: Design of structures for earthquake resistance - Part 1 : general rules, seismic actions and rules for buildings. Brussels: European Committee for Standardization; 2005.
- [18] de Castro J, Keller T. Ductile double-lap joints from brittle GFRP laminates and ductile adhesives, Part I: experimental investigation. *Composites Part B* 2008;39:282–91. <https://doi.org/10.1016/j.compositesb.2007.02.015>.
- [19] Dai Y, Bai Y, Keller T. Stress mitigation for adhesively bonded photovoltaics with fibre reinforced polymer composites in load carrying applications. *Composites Part B* 2019;177:107420. <https://doi.org/10.1016/j.compositesb.2019.107420>.
- [20] Angelidi M, Vassilopoulos AP, Keller T. Ductility, recovery and strain rate dependency of an acrylic structural adhesive. *Construct Build Mater* 2017;140:184–93. <https://doi.org/10.1016/j.conbuildmat.2017.02.101>.
- [21] Eslami G, Movahedi-Rad AV, Keller T. Viscoelastic adhesive modeling of ductile adhesive-composite joints during cyclic loading. *Int J Adhesion Adhes* 2022;119:103241. <https://doi.org/10.1016/j.ijadhadh.2022.103241>.
- [22] ASTM-D1002. Standard test method for apparent shear strength of single-lap-joint adhesively bonded metal specimens by tension loading (Metal-to-Metal). 2019. <https://doi.org/10.1520/D1002-10R19>.
- [23] ASTM-D2651. Standard guide for preparation of metal surfaces for adhesive bonding. 2016. <https://doi.org/10.1520/D2651-01R16>.
- [24] Sika. SikaFast ® -555 L05. <https://industry.sika.com/en/home/appliance-and-equipment/hvac/sikafast-555-l03.html>; 2020.
- [25] Keller T, Rothe J, de Castro J, Osei-Antwi M. GFRP-balsa sandwich bridge deck: Concept, design, and experimental validation. *Compos. Constr.* 2014;18:10–20. [https://doi.org/10.1061/\(ASCE\)CC.1943-5614.0000423](https://doi.org/10.1061/(ASCE)CC.1943-5614.0000423).
- [26] Keller T, Gürtler H. Design of hybrid bridge girders with adhesively bonded and compositely acting FRP deck. *Compos Struct* 2006;74:202–12. <https://doi.org/10.1016/j.compstruct.2005.04.028>.
- [27] Moussa O, Vassilopoulos AP, De Castro J, Keller T. Long-term development of thermophysical and mechanical properties of cold-curing structural adhesives due to post-curing. *J Appl Polym Sci* 2013;127:2490–6. <https://doi.org/10.1002/app.37965>.

- [28] Eslami G, Movahedirad AV, Keller T. Pseudo-ductility in fiber-polymer composites adhesive joints under cyclic loading. Doctoral thesis. EPFL; 2023. <https://doi.org/10.5075/epfl-thesis-10496>.
- [29] Fiberline composites A/S Fiberline Design Manual. 2003. p. 1–326. <https://fiberline.com/design-manual>.
- [30] Krawinkler H, Parisi F, Ibarra L, Ayoub A, Medina R. Development of a testing protocol for woodframe structures, CUREE - Publication No. W-02. 2000.
- [31] D5573-99(2005). Standard practice for classifying failure mode in fiber-reinforced-plastic (FRP). ASTM B. Stand. 2005;99:1–18. <https://doi.org/10.1520/D5573-99R05>.
- [32] Eslami G, Yanes-Armas S, Keller T. Energy dissipation in adhesive and bolted pultruded GFRP double-lap joints under cyclic loading. Compos Struct 2020;248: 112496. <https://doi.org/10.1016/j.compstruct.2020.112496>.
- [33] Grace NF, Soliman AK, Abdel-Sayed G, Saleh KR. Behavior and ductility of simple and continuous FRP reinforced beams. J Compos Construct 1998;2:186–94. [https://doi.org/10.1061/\(asce\)1090-0268\(1998\)2:4\(186\)](https://doi.org/10.1061/(asce)1090-0268(1998)2:4(186)).